Journal of Nuclear Materials 537 (2020) 152191

Contents lists available at ScienceDirect

Journal of Nuclear Materials

journal homepage: www.elsevier.com/locate/jnucmat

Effects of applied strain on defect production and clustering in FCC Ni

Qing Guo , Kan Lai *, Yingjie Tang , Haohua Wen , Biao Wang **

Sino-French Institute of Nuclear Engineering and Technology, Sun Yat-sen University, Zhuhai, 519082, Guangdong, China

ARTICLE INFO

Article history:
Received 5 October 2019
Received in revised form
21 April 2020
Accepted 22 April 2020
Available online 19 May 2020

Keywords:
Molecular dynamics simulation
Collision cascade
Nickel
Strain
Clustering

ABSTRACT

The structural materials of nuclear reactors are subjected to an environment of complex mechanical stresses, which has been reported to significantly affect the primary radiation damage suffered by the structure. In this study, we perform classical molecular dynamics simulations to study the effects of mechanical strains on the defect morphology due to primary radiation damage for a collision energy of 5 keV in face-centered cubic Ni. We consider the effects of four representative types of mechanical strains: hydrostatic, tetragonal shear, monoclinic shear, and uniaxial strains, and we discuss three aspects of the defect morphology: 1) time evolution of generated Frenkel pairs, 2) size distribution of defect clusters, and 3) fraction of clustered defects. We find that volumetric and anisotropic strains differently and significantly influence the primary radiation damage to the structure via affecting the intrinsic physical properties associated with the generation, formation, migration, or binding of Frenkel pairs; this result is generally consistent with those of many simulations. We believe our current study can aid in providing a fundamental mechanistic understanding of primary radiation damage in Ni-based alloys (for e.g., high-entropy alloys) as well as the subsequent long-term microstructural evolution.

1. Introduction

In nuclear fission and fusion reactors, the microstructural evolution of structural materials subjected to irradiation results in the adverse aging/deterioration of their mechanical properties, which can significantly affect the reactor safety and lifetime [1–4]. As the first stage of irradiation damage accumulation, primary radiation damage leads to the generation of numerous Frenkel pairs (FPs), i.e., vacancies and self-interstitials (SIAs), and these defects form the seed of the subsequent long-term evolution of the microstructure. Thus, the mechanistic understanding of primary radiation damage in structural materials is a key issue in nuclear science and engineering.

Nickel (Ni)-based alloys are widely used as structural materials owing to their highly desirable mechanical properties and structural stability [2]. In particular, Ni-based high-entropy alloys (HEAs) have been reported to exhibit good irradiation resistance, which makes them potential candidates for structural materials in next-generation nuclear reactors [5,6].

Against this backdrop, here, we focus on the primary radiation damage of face-centered cubic (FCC) Ni (the prototype system of a large group of Ni-based HEAs), and we study the fundamental mechanism of the microstructural morphology and evolution under irradiation, which can provide insights into the irradiation damage accumulation of Ni-based HEAs.

As is well known, primary radiation damage is associated with a complex non-equilibrium process in a short duration (several picoseconds). However, this process cannot easily be directly observed in experiments. In this context, we note that computer modeling, particularly molecular dynamics (MD) simulation, is a powerful tool to understand the fundamental mechanism of such complex processes [7–10]. Typically, primary radiation damage is investigated by assuming a collision cascade initiated by a primary knock-on atom (PKA) energized by neutrons or other injected particles. In this context, it has been found that external environmental factors (PKA energy, temperature, etc.) and intrinsic pre-existing crystalline defects in the structural materials exert significant influence on the microstructural morphology and evolution arising from primary radiation damage, including the numbers and clustering of the resulting defects and their distribution [10–12]. However, most previous MD simulation studies on collision cascades have been conducted assuming the strain-free condition of the structure, while little attention has been paid to the effects of

* Corresponding author.
** Corresponding author.
E-mail addresses: laik3@mail.sysu.edu.cn (K. Lai), wangbiao@mail.sysu.edu.cn (B. Wang).

https://doi.org/10.1016/j.jnucmat.2020.152191
0022-3115/

mechanical loading. In fact, the structural materials in reactors usually experience an environment of complex mechanical stresses and strains, for e.g., external loading, thermal stress, and strains induced by void swelling and solute precipitation [13,14]. In addition, high density of the extended defects like hydride precipitates and helium bubbles could even induce very high local stress in materials [15].

Mechanical strain has been determined to be a key factor in primary radiation damage; for instance, such strain can change the formation, migration, binding, and threshold displacement energies of radiation-induced defects and thus the microstructural morphology after the collision cascade process. Recent simulations have indicated that different types of applied strains lead to various types of changes in the defect morphology. For example, in body-centered cubic (BCC) metals (e.g., Fe or W), the application of volumetric (for e.g., uniaxial and hydrostatic) strains significantly increases the number of surviving defects [16,17]. However, this is not the case when volume-conserved (e.g., tetragonal and monoclinic shear) strains are applied, because the threshold displacement energy (TDE) and formation energy are more sensitive to changes in the system volume [18,19]. On the other hand, for FCC metals (e.g., Cu), the application of both volumetric and volume-conserved strains can result in the formation of a larger number of survival defect clusters after the cascade process [20,21]. Extended defects such as void and stacking faults can also be generated [22]. Meanwhile, hexagonal close-packed (HCP) metals (e.g., Zr) subjected to the cascade process reportedly exhibit entirely different morphologies. In such metals, the applied uniaxial strains significantly influence the size of the defect clusters, but not the number of surviving defects [23]. However, in all cases, the mechanical loading effects on the primary radiation damage are found to primarily affect the crystalline structure and intrinsic physical properties [11].

Meanwhile, very few simulations have considered the effects of mechanical loading on primary radiation damage in FCC Ni. Such investigations can provide fundamental mechanistic insights into the irradiation damage accumulation of Ni-based alloys (e.g., Ni-based HEAs). Against this backdrop, here, using classical MD simulations, we study the microstructural morphology (defect generation and clustering, size distribution of defect clusters, etc.) induced by collision cascades under various external mechanical strains (hydrostatic, tetragonal shear, monoclinic shear, and uniaxial strains) in FCC Ni to obtain a fundamental mechanistic understanding of the mechanical loading effects on primary radiation damage. The paper is structured as follows: our simulation method is presented in Sec. 2. The results and discussion are presented in Sec. 3, and conclusions are drawn in Sec. 4.

2. Simulation method and details

In the study, we carried out MD simulations using the Large-scale Atomic/Molecular Massively Parallel Simulator (LAMMPS) software package [24]. The many-body potential based on the embedded-atom method (EAM) [25] developed by Bonny and co-workers [26] was adopted to describe the long-range interatomic interactions between Ni atoms, as this approach has been found appropriate for studying primary radiation damage in Ni-based alloys [5,27,28]. The short-range interatomic interactions were described with the use of the Ziegler–Biersack–Littmark (ZBL) universal potential [29] by smooth spline-fitting to the Bonny potential [34].

The simulation supercell contained 50 FCC unit cells along each dimension in the Cartesian coordinate system, including 500,000 Ni atoms, and the periodic boundary condition was applied to avoid surface effects. The system was firstly relaxed to a thermal

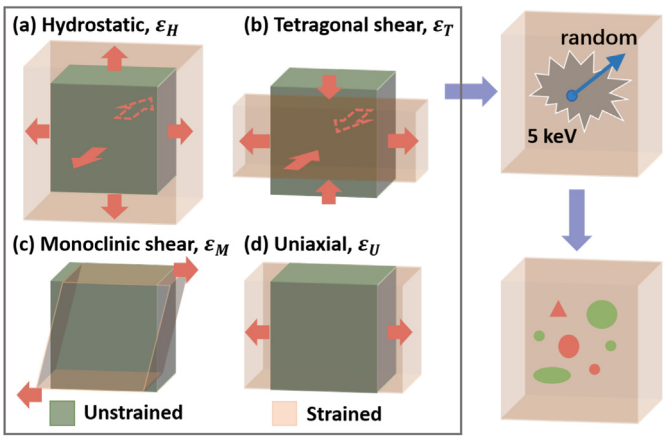

Fig. 1. Schematics of mechanical strains applied to FCC Ni crystal (left) and primary radiation damage (right). Here, four type mechanical strains are considered: (a) hydrostatic ε_H, (b) tetragonal shear ε_T, (c) monoclinic shear ε_M, and (d) uniaxial strains ε_U. The dark green box represents the original FCC crystal, the orange box the strained one, and the red arrow the action of the positive strains applied. (For interpretation of the references to colour in this figure legend, the reader is referred to the Web version of this article.)

equilibrium state under the isothermal-isobaric (NPT) condition for 50 ps, with the temperature fixed at 300 K and the pressure controlled to 0 bar using the Nosé–Hoover thermostat and barostat, respectively [31,32], to obtain the equilibrium lattice constant of 3.551 Å. Here, the phase trajectory was acquired by solving the equations of motion based on the velocity-Verlet approach with the time step set to 2 fs. Next, the system was relaxed under the applied mechanical strains by correspondingly rescaling the supercell for another 100 ps of MD runs to obtain a strained atomic configuration. The schematic in Fig. 1 shows the various types of applied mechanical strains, which form the external environment to the collision cascade process: (a) hydrostatic strain ε_H (from −3% to +2%)[1], (b) tetragonal shear strain ε_T along the [100] direction (from −3% to +4%)[2], (c) monoclinic shear strain ε_M (from 0% to +4%)[3], and (d) uniaxial strain ε_U along the [100] direction (from −5.5% to +4%)[4], with the strain interval being set to 0.5%. Here, we note that the hydrostatic and uniaxial strains are volumetric, while the tetragonal and monoclinic shear strains are volume-conserved.

After the strained atomic configuration was obtained, the cell was subjected to PKA energy by setting the velocity of an atom at center of supercell in random direction. Meanwhile, we have performed additional simulations with a commonly used high-index direction (the [135] direction, defined in the original supercell) for all strains, corresponding results are presented in the Supplementary Materials Fig. S1, Fig. S2, and Fig. S3. Here, the velocity is set to the value corresponding to the kinetic energy of 5 keV, which is the typical recoil energy in collision cascade simulations [16,33]. The collision cascade is simulated in an NVE ensemble while the outer two atomic layers of the supercell in an NVT ensemble where the temperature is set as 300 K with Berendsen thermostat to extract heat from system [33,34]. In the final step, the system was relaxed for at least 20 ps by application of a variable time step

[1] '+' ('-') denotes elongation (compression) of the supercell in three dimensions.
[2] '+' ('-') denotes elongation (compression) of the supercell in the [100] direction with compression (elongation) along both the [010] and [001] directions.
[3] '+' denotes change in the xy tilt factor.
[4] '+' ('-') denotes elongation (compression) of the supercell along the [100] direction.

algorithm, wherein the time step was constrained to limit the maximum atomic displacement to 0.01 Å for each MD integration step [36]. The irradiated phase trajectory was acquired for defect analysis as below: To limit the statistical error, each scenario was repeated for 50 independent MD simulations.

After the MD run and obtainment of the phase trajectory, defect identification was performed with the use of displaced atom (D-A) analysis [37]. As per the analysis, a sphere centered on an arbitrary perfect lattice site with a radius of 0.27 lattice constant [34] was used to define the spacing occupied by a regular atom; consequently, any atom that did not locate within these spheres was identified as an interstitial, and a sphere with a missing atom was identified as a vacancy. In addition, cluster analysis was carried out using the first-nearest-neighbor (1NN) distance for SIAs. It has been checked that varying the cutoff from 1NN to 4NN did not alter the qualitative results (shown in the Supplementary Materials Fig. S4). All the visual images were prepared using the Visual Molecular Dynamics (VMD) software package [38].

3. Results and discussion

Primary radiation damage is induced by a collision cascade initiated with a high-energy PKA. Three aspects are usually considered in simulations to characterize the defect morphology induced by primary radiation: 1) evolution of FPs (N_{FP}); 2) size distribution of defect clusters; and 3) fraction of clustered defects. Here, we note that the details of the defect morphology due to collision cascades are considered as important input parameters of computer modeling models developed for the long-term evolution of irradiation damage accumulation, for e.g., kinetic Monte Carlo (KMC) or rate equations (RE, or reaction rate theory) [39]. In this section, considering the results under the strain-free condition as the reference, we discuss the effects of the various mechanical strains on the three above mentioned aspects in our study of primary radiation damage in FCC Ni.

3.1. Time evolution of number of Frenkel pairs

During the cascade process, numerous FPs are generated due to the energy and momentum transferred from the high-energy PKA to the atoms within the material of interest. According to the FP generation rate, the collision cascade process can be divided into the ballistic stage and thermally enhanced recovery stage [40]. Fig. 2a and Fig. 2b show, respectively, the time-dependent number of FPs $N_{FP} = N_{FP}(t)$ generated within the crystalline solid from the instance of PKA injection and the corresponding effective generation rate $\Gamma_{FP}(t)$ for FCC Ni under the strain-free condition. The generation rate is defined as

$$\Gamma_{FP}(t) = \frac{d\log_{10}N}{d\log_{10}t} \quad (1)$$

From Fig. 2a, we observe that N_{FP} increases rapidly and reaches its maximum value (N_{peak}) of ~ 4000 in the ballistic phase, whose duration is very short (~ 0.5 ps), as measured from the instance of 5 keV PKA injection. On the other hand, in the ballistic phase, the generation rate of FPs (Γ_{FP}) shown in Fig. 2b is the highest in the first ~ 0.1 ps, namely, the supersonic phase, and the rate then reduces to zero from 0.1 ps until the end of ballistic phase; this reduction interval corresponds to the sonic phase [37]. Here, we note that recoils occur because the PKA kinetic energy is significantly larger than the TDE, which results in a supersonic shockwave traveling inside the crystal [37,41]. In this supersonic phase, a large number of neighboring atoms gain sufficient energy to leave their lattice sites, which leads to the rapid increase in N_{FP}; these FPs form

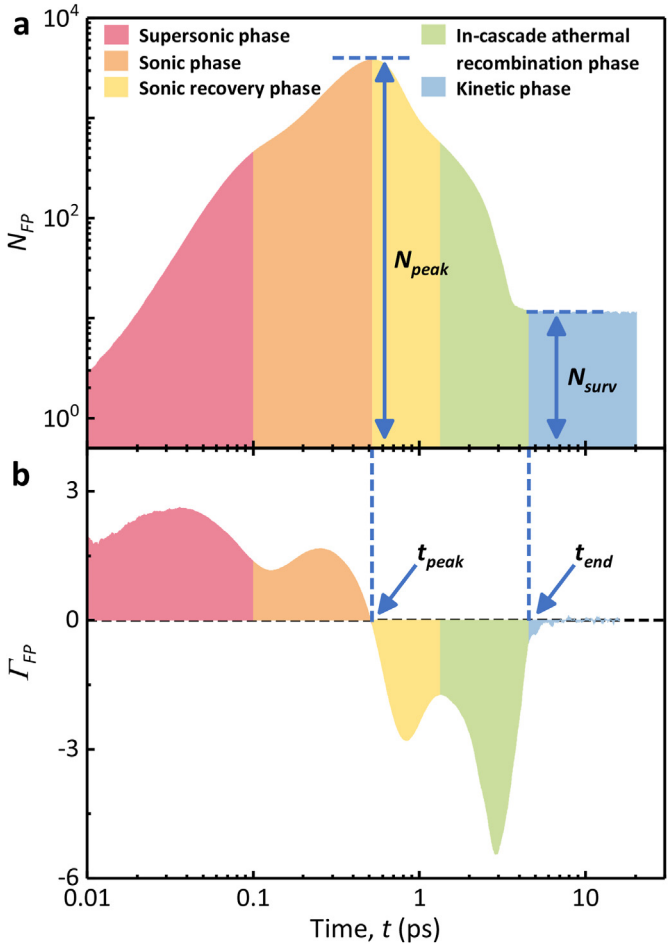

Fig. 2. (a) Time dependence of number of generated Frenkel pairs $N_{FP}(t)$ and (b) effective generation rate $\Gamma_{FP}(t)$ induced by 5 keV PKA injection into FCC Ni at 300 K. The non-equilibrium cascade process can be divided into five phases as a function of the elapsed time. The red region represents the supersonic phase, orange the sonic phase, yellow the sonic recovery phase, green the in-cascade athermal recombination phase, and blue the kinetic phase. (For interpretation of the references to colour in this figure legend, the reader is referred to the Web version of this article.)

the seeds of permanent defects in primary radiation damage. Meanwhile, atoms that are distant from the PKA cannot gain sufficient energy to leave their lattice sites permanently after the attenuation of the supersonic shockwave [42,43], which leads to a gradual Γ_{FP} reduction in the subsequent interval up to ~ 0.5 ps; this phase is called the sonic phase, as shown in Fig. 2. Here, the time instant of ~ 0.5 ps, when $N_{FP} = N_{peak}$, is defined as the peak time (t_{peak}). In general, the damage in the supersonic phase is destructive, while that in the sonic phase is nondestructive [37,43]. Therefore, beyond t_{peak}, the transiently displaced atoms return to their lattice sites, which corresponds to a negative Γ_{FP}, i.e., a reduction in N_{FP}. This phase is what we called the sonic recovery phase of the thermally enhanced recovery stage, corresponding to the interval of 0.5 ps $< t <$ 1.2ps. Subsequently, FPs recover because of the strong intrinsic strain field induced by the strong lattice disorder that persists at the core of the cascade; thus, Γ_{FP} increases to zero at the end of the cascade (t_{end}, corresponding to ~ 5 ps in Fig. 2). After the cascade, the system tends to reach a thermal equilibrium state, i.e. the kinetic phase, and N_{FP} remains constant, which is referred to as the number of surviving FPs (N_{surv}).

Fig. 3 plots the time-evolution behaviors of FPs generation under various types of mechanical strains: (a) hydrostatic strain ε_H, (b)

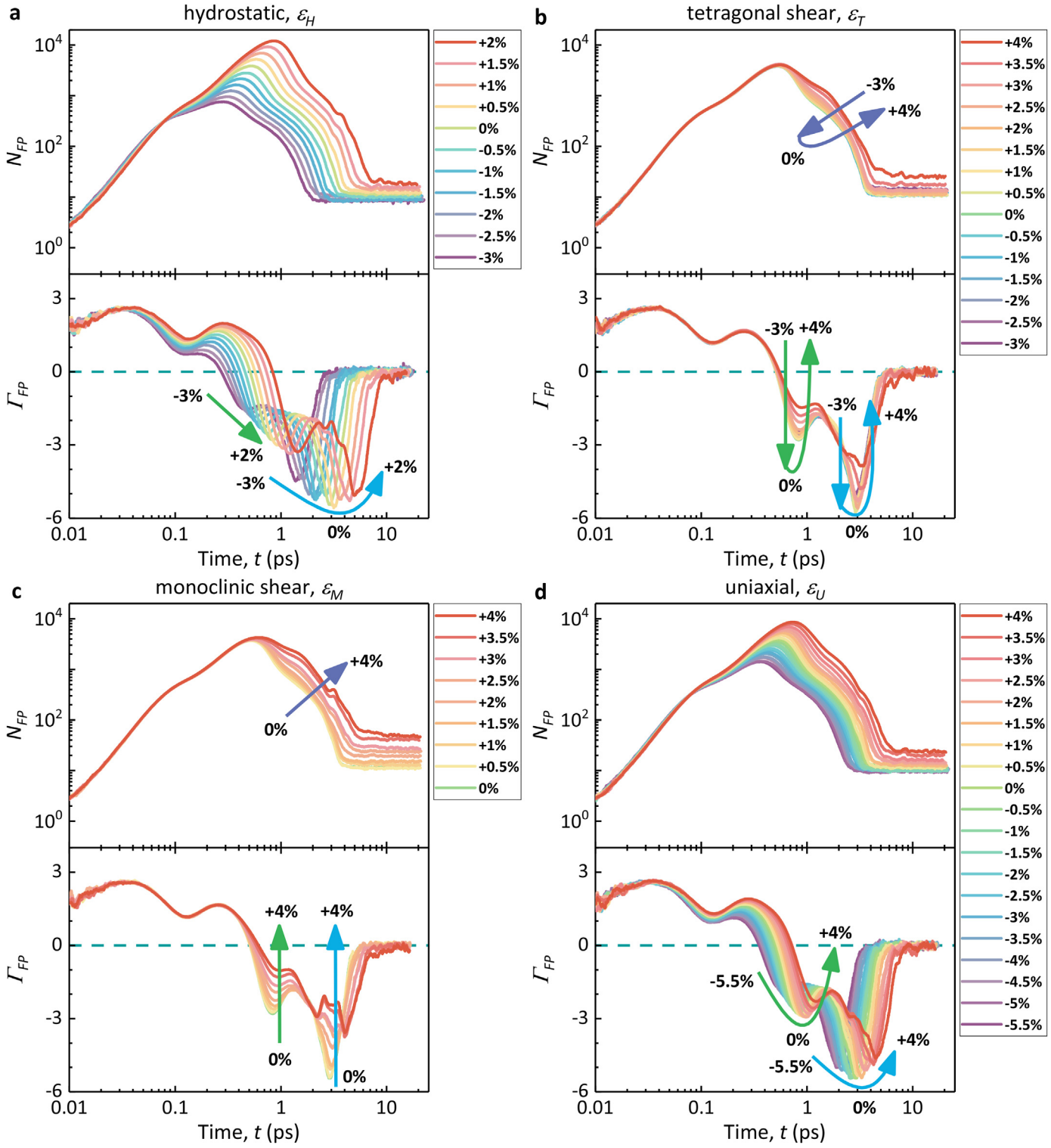

Fig. 3. Time dependence of number of generated Frenkel pairs N_{FP} and effective generation rate Γ_{FP} of FCC Ni under various applied mechanical strains: (a) hydrostatic ε_H, (b) tetragonal shear ε_T, (c) monoclinic shear ε_M, and (d) uniaxial strains ε_U. The arrows indicate the corresponding tendencies.

tetragonal shear strain ε_T, (c) monoclinic shear strain ε_M, and (d) uniaxial strain ε_U. Upon comparing the results between the strained and strain-free conditions, we were able to analyze the effects of the mechanical strains. Here, keeping in mind the different mechanisms affecting the N_{FP} and Γ_{FP} values, we discuss the effects according to the various phases of primary radiation damage.

(1) In the supersonic phase, which is assumed to be an adiabatic process, the primary radiation damage is mainly determined by the injected PKA energy [42], and we found that it is independent with the applied strains. That is, all the applied strains negligibly influence N_{FP} and Γ_{FP} (Fig. 3), and the duration.

(2) In the sonic phase, as reported in literature, the kinetic energy of the fastest atom in the system is lower than the TDE, thereby leading to temporary atomic displacements [43]. Here, we note that the TDE value is closed related to atomic interactions and the local environment. Therefore, the volume-conserved strains, i.e., ε_T and ε_M in the current work, do not significantly influence N_{FP} and Γ_{FP}, as well as the elapsed time t_{peak} to reach the maximum N_{FP} value. On the other hand, the application of ε_H and ε_U results in the changes to the system volume, thus significantly affecting N_{FP} and Γ_{FP}, as shown in Fig. 3a and d. In particular, when compared with the case of ε_U, the degree of volume contraction is stronger for ε_H, which corresponds to a greater increase in N_{FP} and larger value of t_{peak}. In addition, while the TDE is enhanced with reduction in the system volume, it is only slightly affected by anisotropic deformation [18,19,44]. Therefore, the application of positive strains gives rise to enhanced FP generation. Moreover, the duration of sonic phase (and the time taken to reach the maximum N_{FP} value) increases, which can be clearly observed in Fig. 3a and d.

(3) In the sonic recovery phase, the temporarily displaced atoms return to their lattice sites with sonic-shockwave dissipation. In this phase, the volumetric change and anisotropic deformation of the crystal are revealed to affect the recovery of FPs in different ways. In Fig. 3a, we note that Γ_{FP} increases to large values with the isotropic increase in volume resulting from ε_H application, similar to the case of the sonic phase. On the other hand, the application of volume-conserved shear strains, i.e., ε_T and ε_M (Fig. 3b and c) also significantly influences Γ_{FP}, which suggests that anisotropic deformation should be taken into account. Meanwhile, the application of ε_U results in a complicated Γ_{FP} evolution behavior: the recovery of FPs is enhanced with increasing volume and restrained by anisotropic deformation (Fig. 3d).

(4) In the in-cascade athermal recombination phase, the vacancies and SIAs undergo recombination to reduce N_{FP}. The application of positive strains suppresses this decreasing trend, regardless of whether they are volumetric or volume-conserved strains. A similar trend is observed even under negative strains, which indicates that both volumetric change and shear deformation degrade the FP recovery and increase the time consumption. Here, the increase in Γ_{FP} under anisotropic strains (i.e., ε_T, ε_M, and ε_U) in the sonic recovery phase and the in-cascade athermal recombination phase can be attributed to change in the diffusion mode of the SIAs; SIAs "prefer" one-dimensional migration over three-dimensional migration under anisotropic strain [45].

(5) In the kinetic phase, the damaged system finally reaches a thermal equilibrium state, and the number of surviving FPs (N_{surv}) is related to the defect morphology resulting from the non-equilibrium process in the collision cascade. Besides, previous researches of the temperature effect have indicated that the application of high temperature extends the cascade lifetime, thereby leading to greater defect recovery and the formation of less stable FPs [46,47]. However, in this study, large t_{end} values afford greater N_{surv}. We posit that higher positive strains directly generate extended defect structures, thereby resulting in the formation of more stable FPs.

In this section, we briefly discuss the above results. In the ballistic stage, N_{peak} is sensitive to the volume change $\omega = V(\varepsilon)/V(0) - 1$, induced by either ε_H or ε_U, but nearly independent of volume-conserved mechanical loading. This can be confirmed by examining the plot shown in the inset of Fig. 4a, wherein N_{peak} shows a well-defined volumetric-strain dependence; this result indicates that N_{peak} remains unchanged when the volume is unchanged, regardless of whichever type of strain is applied. Meanwhile, from the relation between N_{peak} and ε (Fig. 4a), we note that the volume-conserved strains hardly influence N_{peak}. According to the conjecture that TDE varies positively with change in the average atomic volume of materials, we conclude that the damage in the ballistic stage is mainly determined by the TDE, which is a function of the applied volumetric strain.

3.2. Surviving FPs

In the thermally enhanced recovery stage, the volume change and anisotropic deformation induced by strain application exert significant but different effects on the structure. In Fig. 4b, we plot N_{surv} as a function of the strains and N_{surv} as a function of volume change in the inset. These plots indicate a different relationship from that shown in Fig. 4a for each strain. For instance, N_{surv} exhibits an increasing trend with the volume increase induced by ε_H. However, the change in N_{surv} with the volume change under ε_U is more significant relative to ε_H (inset of Fig. 4b), which indicates that the anisotropic deformation reduces the FP recovery, thus increases N_{surv}. Such effects of anisotropic deformation can be also observed for the results corresponding to ε_T and ε_M application; the applied volume-conserved strains give rise to significant variation in N_{surv}. The different effects between the volumetric strains and anisotropic deformation can be clearly observed in Fig. 4b, wherein N_{surv} increases upon application of the pure anisotropic strains, i.e., both positive and negative ε_T and positive ε_M.

Furthermore, the volume compression induced by the application of negative ε_H suppresses N_{surv}, while expansion affords an increase in N_{surv}. In particular, for negative ε_U, the effect of negative anisotropic deformation on N_{surv} is in competition with that of volume compression, and both these effects appear to cancel each other; on the other hand, for positive ε_U values, both anisotropic deformation and volume expansion enhance the growth of N_{surv}. Here, we note that similar effects of anisotropic deformation have been reported for FCC Cu [21], but not for BCC Fe [16], which suggests that the recovery ability of materials under irradiation depends on their crystalline structure [11]. Moreover, the closed-packed structure appears to be more sensitive to anisotropic deformation. In addition, we compare the results of random and [135] directions. It is found that the results of these two set of PKA directions show little difference, the conclusions are consistent. Detailed comparative information is provided in the Supplementary Materials Fig. S1, Fig. S2, and Fig. S3.

Finally, to consider how both N_{peak} and N_{surv} change with the applied strains, we propose the use of the so-called survival rate r to characterize the recovery ability of materials [16]:

$$r(\varepsilon) = N_{surv}(\varepsilon) \Big/ N_{peak}(\varepsilon) \tag{2}$$

Here, we note that smaller r values correspond to greater recombination abilities. The relation between r and applied strain ε (volume change ω) is plotted in Fig. 4c (inset of Fig. 4c). We find that r decreases with increase in the volume of FCC Ni under ε_H, which indicates that a larger local atomic spacing aids FP recovery. However, we observe an anomalous "U-shaped" relation under ε_U application relative to the results under ε_H application, which suggests that anisotropic deformation significantly suppresses FP recovery. This hypothesis can be confirmed from the plot of r vs. ε_M in Fig. 4c, wherein r exhibits a progressively increasing trend with increase in ε_M. Furthermore, r is only slightly affected by anisotropic deformation under ε_T application.

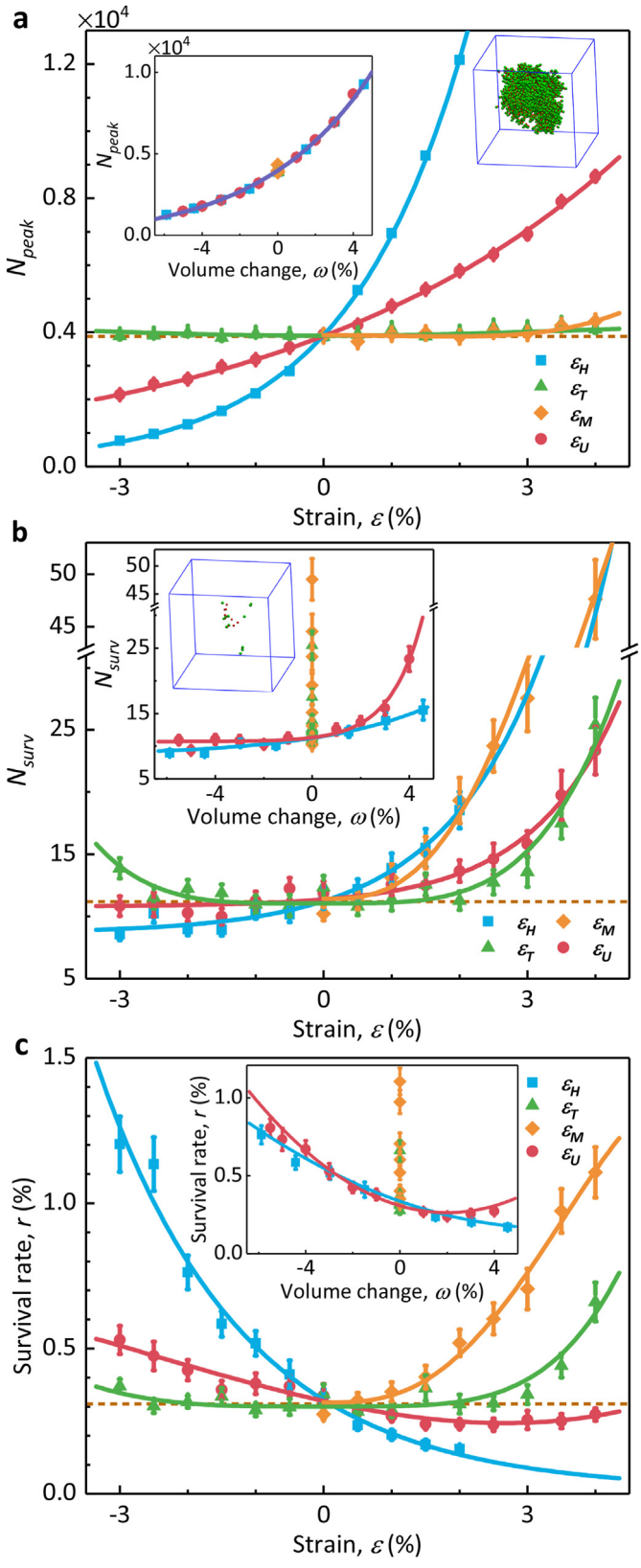

Fig. 4. (a) Peak number of Frenkel pairs (FPs, N_{peak}), (b) number of surviving FPs (N_{surv}), and (c) survival rate of FPs (N_{surv}/N_{peak}) in FCC Ni as functions of applied mechanical strains: hydrostatic ε_H, tetragonal shear ε_T, monoclinic shear ε_M, and uniaxial strains ε_U. The corresponding insets show the relation between each of the three characteristics and the volume change. Here, the lines in the figures are plotted for visual guidance, and the error bars denote the standard error. The red spheres in the cube denote vacancies and green ones denote self-interstitials (SIAs).

3.3. Size distribution of defect-clusters

In the previous section, we discussed the effects of mechanical strains on the number of FPs generated and the FPs surviving the collision cascade process to examine the primary radiation damage in FCC Ni. In this section, we focus on the formation of defect clustering, which is one of the most important aspects of the defect morphology induced by PKAs. Here, we note that because the size of vacancy clusters is extremely small under 5 keV PKA injection, we only discuss the interstitial clusters here. For convenience, according to the number of interstitials n, we categorized the observed clusters into six size ranges: $n \leq 2$, $3 \leq n \leq 6$, $7 \leq n \leq 11$, $12 \leq n \leq 19$, $20 \leq n \leq 32$, and $n > 32$ (Fig. 5). In particular, the cluster with $n \leq 2$ corresponds to single SIAs or dumbbells, while the cluster corresponding to the interval of $3 \leq n \leq 11$ is called a small-size cluster. Similarly, the cluster corresponding to $12 \leq n \leq 19$ is named a medium-size cluster, and that corresponding to $20 \leq n \leq 32$ is a large-sized cluster. Finally, the cluster containing 33 or more interstitials is defined as an oversized cluster.

(1) For the cases of pure volumetric deformation induced by ε_H, clusters with $n \leq 6$ are dominant. From Fig. 5a, we note that the large volume resulting from increase in the strain reduces the fraction of single SIAs and dumbbells with $n \leq 2$ and enhances the fraction of clusters with $n \geq 7$. For example, the fraction of single interstitials decreases from $\sim$ 60% for the value $\varepsilon_H = -3\%$ to $\sim$ 20% when $\varepsilon_H = +2\%$. In particular, the fractions of single SIAs and dumbbells decrease rapidly with volume expansion ($0 < \varepsilon_H < +2\%$), wherein the SIAs preferentially form clusters with larger sizes.

(2) For the case of tetragonal shear deformation induced by ε_T (Fig. 5b), small-sized clusters ($7 \leq n \leq 11$) are predominant when compared with the ε_H case. In addition, as regards the single SIA and dumbbells, this fraction decreases regardless of the application of positive or negative ε_T, and the fraction of larger-sized clusters ($n \geq 12$) increases, corresponding to the "U-shaped" trend observed in the figure.

(3) As regards the monoclinic shear deformation induced by ε_M (Fig. 5c), small-sized clusters ($n \leq 11$) are dominant when $\varepsilon_M < +2\%$, and larger-sized ones ($n \geq 12$) are easily formed when the applied ε_M values are large.

(4) For the cases of ε_U, the cluster size distribution exhibits a mixture of the distribution features induced by ε_H and ε_T (Fig. 5d). For example, the fraction of single SIAs and dumbbells rapidly decreases with increase in ε_U in the case of volume expansion. For the fraction of the medium-size cluster, we observe a "U-shaped" behavior similar to the case of ε_T.

From these results, we find that volumetric deformation and anisotropic volume-conserved deformation differently affect the size distribution of the SIA clusters. According to previous studies, the size distribution is mainly determined by the fact that ε changes the formation energy E_f [16] and migration energy E_m [48] of freely moving FPs. For example, E_f shows a decreasing trend with increase in the system volume, induced either by ε_H or ε_U, and therefore, freely moving SIAs are more easily generated. Moreover, the reduction in E_m due to the volume expansion results in an increasing number of clusters. Therefore, the fraction of smaller clusters decreases with increasing volume, and a larger number of large-sized clusters are formed. On the other hand, the anomalous defect morphology induced by anisotropic deformation under ε_T has also been reported in FCC Cu [20]. Here, we

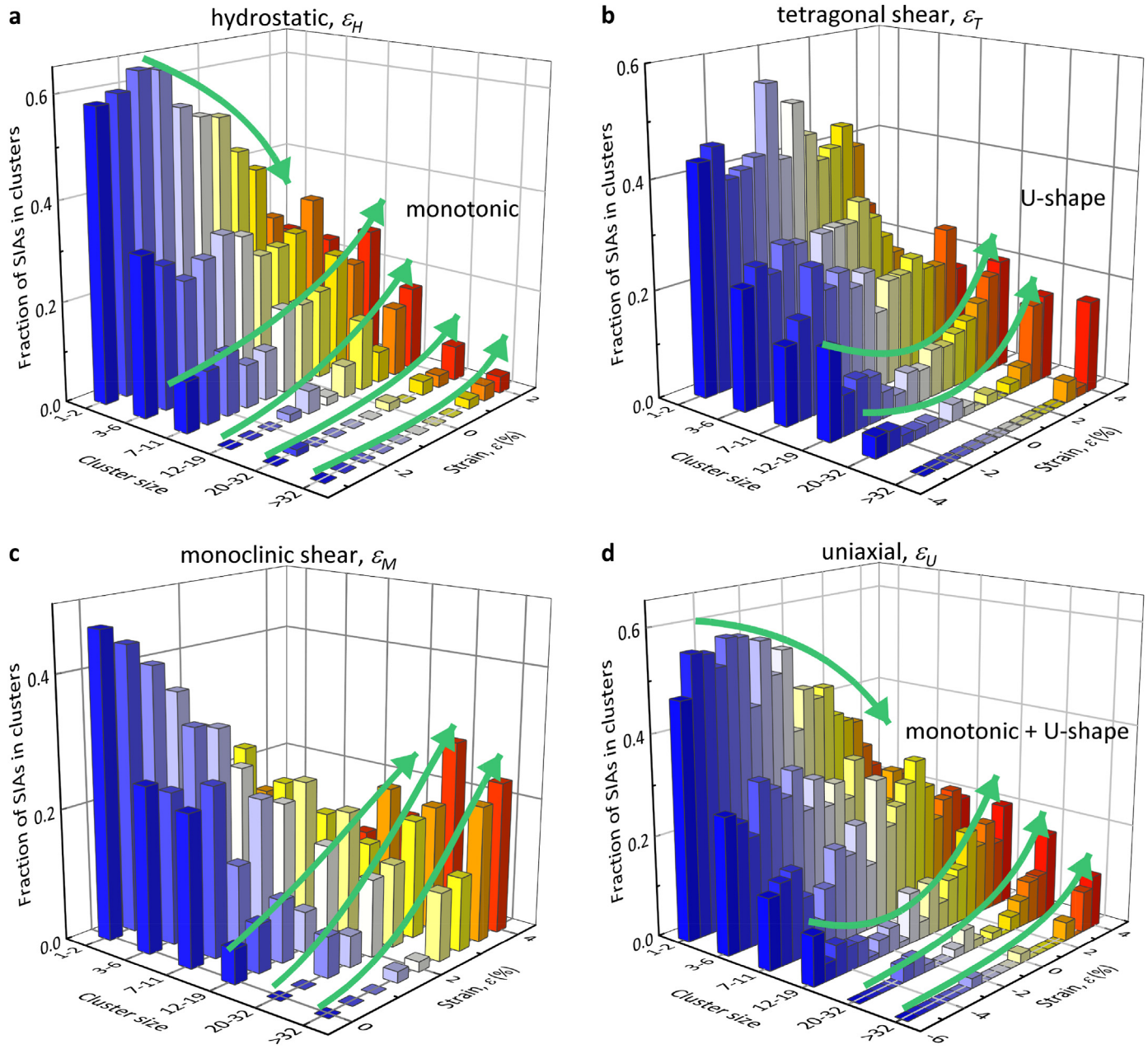

Fig. 5. Size distribution of SIA clusters in FCC Ni subjected to applied mechanical strains: (a) hydrostatic ε_H, (b) tetragonal shear ε_T, (c) monoclinic shear ε_M, and (d) uniaxial strains ε_U. The arrows indicate the distribution tendencies.

note that clustering behavior is suggested to be related to the binding energy [11]. However, in this study, the difference in binding energy under various strain types might be too small to affect short-duration single-cascade events; thus, the effect of strain on the binding energy needs further investigation. From our findings, we can conclude that volumetric change and anisotropy are both key factors affecting the size distribution of clusters; for instance, expansion induces defect clustering, thereby leading to the formation of a reduced number of point defects, whereas the destruction of cubic symmetry also promotes clustering.

3.4. Fraction of clustered defects

In addition to the size distribution of clusters, the fraction of SIA clustering is also considered a key aspect that can shed light on the defect morphology. Here, the fraction of SIA clustering is defined as the ratio of the number of clustered SIAs (number of SIAs in a cluster of $n \geq 9$) to the total number of surviving SIAs. From Fig. 6, we find that mechanical loading significantly affects SIA aggregation. For the volumetric deformation induced by ε_H, the SIA clustering fraction exhibits a progressively increasing trend from negative values to positive values with increasing ε_H,

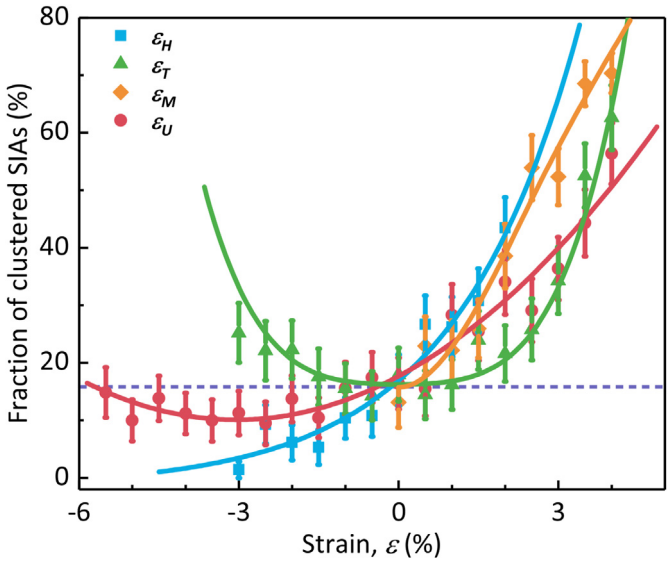

Fig. 6. Fraction of clustered SIAs in FCC Ni as function of applied mechanical strains: hydrostatic ε_H, tetragonal shear ε_T, monoclinic shear ε_M, and uniaxial strains ε_U. The lines in the figure are plotted for visual guidance, and the error bars denote the standard error.

thereby indicating that the volume expansion favors defect clustering. However, a similar "U-shaped" behavior of the clustering fraction is also observed in the case of ε_T, which suggests that anisotropic deformation, either positive or negative, also enhances defect clustering. A similar behavior can be observed in the case of ε_M as well. Moreover, the competition between volume compression and anisotropic deformation determines the behavior of clustering upon applying negative ε_U strain. From Fig. 6, we note that under small uniaxial strains (for e.g., $\varepsilon_U > -3\%$), the reduction in SIA clustering due to volume compression is dominant, while the enhancement due to anisotropic deformation is comparable with volume compression when $\varepsilon_U < -3\%$. Here, we note that as discussed in the previous section, the interactions between SIAs determine their aggregation, wherein the strain forms a significant factor. However, because the difference in binding energy between SIAs induced by applied strains might be very small relative to the energy of thermal fluctuations during a single cascade event, the difference cannot be easily estimated [11]. Moreover, the SIA clustering behavior is believed to be more pronounced under higher doses of irradiation (for e.g., higher recoil energy or damage accumulation by overlapping cascades); thus, the fundamental mechanism underlying defect clustering requires further investigations.

4. Conclusions

We utilized MD simulations to study the effects of mechanical strains on the defect morphology of the primary radiation damage occurring in FCC Ni for radiation with a collision energy of 5 keV. Four representative types of mechanical strains were considered: hydrostatic ε_H, tetragonal shear ε_T, monoclinic shear ε_M, and uniaxial strains ε_U, which resulted in purely volumetric (by ε_H), volume-conserved anisotropic (by ε_T and ε_M) and volumetric anisotropic deformation (by ε_U) (schematically shown in Fig. 7). Furthermore, we discussed three important aspects of the defect morphology: 1) time evolution of the generated FPs; 2) size distribution of defect clusters, and 3) fraction of clustered defects. Our findings show that volumetric strains induce volume changes and consequently affect the TDE and the number of FPs generated, for e.g., volume expansion enhances the range of radiation damage in the ballistic stage of the collision cascade process. On the other hand, both volumetric and anisotropic deformations induced by applied mechanical strains significantly influence the recovery of FPs in the thermally enhanced recovery stage and consequently the number of surviving FPs. Furthermore, the enlargement in volume due to applied ε_H or ε_U favors the clustering of self-interstitials; and vice versa. Moreover, the anisotropic deformation induced by positive or negative applied strains gives rise to more SIA clusters. Finally, from the results of the fraction of clustered SIAs, we demonstrate the presence of the competing effect between volumetric deformation and anisotropic deformation, which gives rise to a complicated defect morphology. Our findings clearly indicate that the applied mechanical strains significantly affect the primary radiation damage and the subsequent microstructural evolution along expected lines.

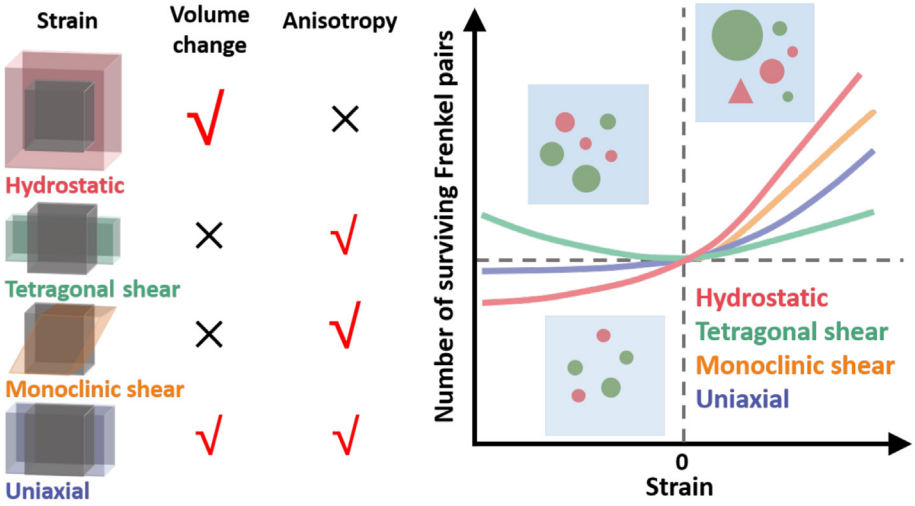

Fig. 7. Schematic of mechanical strains applied to FCC Ni crystal denoting volume change and anisotropy (left panel) and radiation damage to the system under strain (right). The green spheres in the cluster configuration denote interstitials, and the red ones denote vacancies. (For interpretation of the references to colour in this figure legend, the reader is referred to the Web version of this article.)

Declaration of competing interest

The authors declare that they have no known competing financial interests or personal relationships that could have appeared to influence the work reported in this paper.

CRediT authorship contribution statement

Qing Guo: Conceptualization, Data curation, Methodology, Software, Writing - original draft. **Kan Lai:** Conceptualization, Funding acquisition, Supervision, Writing - original draft. **Yingjie Tang:** Methodology, Software. **Haohua Wen:** Writing - review & editing. **Biao Wang:** Project administration, Resources.

Acknowledgements

The authors gratefully acknowledge Dr. Chunyu Zhang, Dr. Yangzhong Li, Kangming Li, and Guo Zhang for insightful discussions. This work was supported by the National Natural Science Foundation of China under Grant No. 11602311, No. 11672339, No. 11602310 Natural Science Foundation of Guangdong Province, China under Grant No. 2014A030310165, Guangzhou Science and Technology Project No. 201707020002 and Special Program for Applied Research on Super Computation of the NSFC-Guangdong Joint Fund (the second phase).

Appendix A. Supplementary data

Supplementary data to this article can be found online at https://doi.org/10.1016/j.jnucmat.2020.152191.

References

[1] S.J. Zinkle, J.T. Busby, Structural materials for fission & fusion energy, Mater. Today 12 (11) (2009) 12–19.
[2] S.J. Zinkle, G.S. Was, Materials challenges in nuclear energy, Acta Mater. 61 (3) (2013) 735–758.
[3] G.S. Was, Fundamentals of Radiation Materials Science: Metals and Alloys, Springer, 2016.
[4] D.J. Hill, Nuclear energy for the future, Nat. Mater. 7 (1) (2008) 680–682.
[5] C. Lu, L. Niu, N. Chen, K. Jin, T. Yang, P. Xiu, Y. Zhang, F. Gao, H. Bei, S. Shi, Enhancing radiation tolerance by controlling defect mobility and migration pathways in multicomponent single-phase alloys, Nat. Commun. 7 (2016) 13564.
[6] K. Jin, C. Lu, L. Wang, J. Qu, W. Weber, Y. Zhang, H. Bei, Effects of compositional complexity on the ion-irradiation induced swelling and hardening in Ni-containing equiatomic alloys, Scripta Mater. 119 (2016) 65–70.
[7] R.E. Stoller, Primary radiation damage formation in metals, in: Reference Module in Materials Science and Materials Engineering, Elsevier, 2016.
[8] K. Nordlund, A.E. Sand, F. Granberg, S.J. Zinkle, R. Stoller, R.S. Averback, T. Suzudo, L. Malerba, F. Banhart, W.J. Weber, F. Willaime, S. Dudarev, D. Simeone, Primary Radiation Damage in Materials, OECD Nuclear Energy Agency, 2015.
[9] D.J. Bacon, F. Gao, Y.N. Osetsky, Atomic-scale computer simulation of primary irradiation damage effects in metals, J. Comput. Aided Mater. Des. 6 (2) (1999) 225–237.
[10] L. Malerba, Molecular dynamics simulation of displacement cascades in α-Fe: a critical review, J. Nucl. Mater. 351 (1) (2006) 28–38.
[11] D.J. Bacon, F. Gao, Y.N. Osetsky, The primary damage state in fcc, bcc and hcp metals as seen in molecular dynamics simulations, J. Nucl. Mater. 276 (1) (2000) 1–12.
[12] X.M. Bai, A.F. Voter, R.G. Hoagland, M. Nastasi, B.P. Uberuaga, Efficient annealing of radiation damage near grain boundaries via interstitial emission, Science 327 (5973) (2010) 1631–1634.
[13] A.D. Brailsford, R. Bullough, The rate theory of swelling due to void growth in irradiated metals, J. Nucl. Mater. 44 (2) (1972) 121–135.
[14] P. Auger, P. Pareige, S. Welzel, J.C.V. Duysen, Synthesis of atom probe experiments on irradiation-induced solute segregation in French ferritic pressure vessel steels, J. Nucl. Mater. 280 (3) (2000) 331–344.
[15] A. Barrow, A. Korinek, M. Daymond, Evaluating zirconium zirconium hydride interfacial strains by nano-beam electron diffraction, J. Nucl. Mater. 432 (1) (2013) 366–370.
[16] B. Beeler, M. Asta, P. Hosemann, N. Grønbech-Jensen, Effects of applied strain on radiation damage generation in body-centered cubic iron, J. Nucl. Mater. 459 (2015) 159–165.
[17] D. Wang, N. Gao, Z.G. Wang, X. Gao, W.H. He, M.H. Cui, L.L. Pang, Y.B. Zhu, Effect of strain field on displacement cascade in tungsten studied by molecular dynamics simulation, Nucl. Instrum. Methods Phys. Res. B 384 (2016) 68–75.
[18] B. Beeler, M. Asta, P. Hosemann, N. Grønbech-Jensen, Effect of strain and temperature on the threshold displacement energy in body-centered cubic iron, J. Nucl. Mater. 474 (2016) 113–119.
[19] D. Wang, N. Gao, W. Setyawan, R.J. Kurtz, Z.G. Wang, X. Gao, W.H. He, L.L. Pang, Effect of strain field on threshold displacement energy of tungsten studied by molecular dynamics simulation, Chin. Phys. Lett. 33 (9) (2016), 096102.
[20] S. Miyashiro, S. Fujita, T. Okita, MD simulations to evaluate the influence of applied normal stress or deformation on defect production rate and size distribution of clusters in cascade process for pure Cu, J. Nucl. Mater. 415 (1) (2011) 1–4.
[21] S. Miyashiro, S. Fujita, T. Okita, H. Okuda, MD simulations to evaluate effects of applied tensile strain on irradiation-induced defect production at various pka energies, Fusion Eng. Des. 87 (7) (2012) 1352–1355.
[22] B. Li, L. Wang, W.R. Jian, J.C. E, H.H. Ma, S.N. Luo, Irradiation-initiated plastic deformation in prestrained single-crystal copper, Nucl. Instrum. Methods Phys. Res. B 368 (2016) 60–65.
[23] S. Di, Z. Yao, M.R. Daymond, F. Gao, Molecular dynamics simulations of irradiation cascades in alpha-zirconium under macroscopic strain, Nucl. Instrum. Methods Phys. Res. B 303 (2013) 95–99.
[24] S. Plimpton, Fast parallel algorithms for short-range molecular dynamics, J. Comput. Phys. 117 (1) (1995) 1–19.
[25] M.S. Daw, M.I. Baskes, Embedded-atom method: derivation and application to impurities, surfaces, and other defects in metals, Phys. Rev. B 29 (1984) 6443–6453.
[26] G. Bonny, N. Castin, D. Terentyev, Interatomic potential for studying ageing under irradiation in stainless steels: the FeNiCr model alloy, Model. Simulat. Mater. Sci. Eng. 21 (8) (2013), 085004.
[27] C. Lu, T. Yang, J. Ke, G. Ning, P. Xiu, Y. Zhang, G. Fei, H. Bei, W.J. Weber, S. Kai, Radiation-induced segregation on defect clusters in single-phase concentrated solid-solution alloys, Acta Mater. 127 (2017) 98–107.
[28] D.S. Aidhy, C. Lu, K. Jin, H. Bei, Y. Zhang, L. Wang, W.J. Weber, Point defect evolution in Ni, NiFe and NiCr alloys from atomistic simulations and irradiation experiments, Acta Mater. 99 (2015) 69–76.
[29] J.F. Ziegler, J.P. Biersack, U. Littmark, The Stopping and Ranges of Ions in Matter, 1985. Pergamon.
[31] S. Nosé, A unified formulation of the constant temperature molecular dynamics methods, J. Chem. Phys. 81 (1) (1984) 511–519.
[32] W.G. Hoover, Canonical dynamics: equilibrium phase-space distributions, Phys. Rev. A 31 (1985) 1695–1697.
[33] M.W. Ullah, Y. Zhang, N. Sellami, A. Debelle, H. Bei, W.J. Weber, Evolution of irradiation-induced strain in an equiatomic NiFe alloy, Scripta Mater. 140 (2017) 35–39.
[34] K. Vrtler, N. Juslin, G. Bonny, L. Malerba, K. Nordlund, The effect of prolonged irradiation on defect production and ordering in Fe–Cr and Fe–Ni alloys, J. Phys. Condens. Matter 23 (35) (2011) 355007.
[36] M. Jin, C. Permann, M.P. Short, Breaking the power law: multiscale simulations of self-ion irradiated tungsten, J. Nucl. Mater. 504 (2018) 33–40.
[37] A.F. Calder, D.J. Bacon, A.V. Barashev, Y.N. Osetsky, On the origin of large interstitial clusters in displacement cascades, Philos. Mag. 90 (7–8) (2010) 863–884.
[38] W. Humphrey, A. Dalke, K. Schulten, Vmd: visual molecular dynamics, J. Mol. Graph. 14 (1) (1996) 33–38.
[39] K. Nordlund, Historical review of computer simulation of radiation effects in materials, J. Nucl. Mater. 520 (2019) 271–295.
[40] D.J. Bacon, A.F. Calder, F. Gao, V.G. Kapinos, S.J. Wooding, Computer simulation of defect production by displacement cascades in metals, Nucl. Instrum. Methods Phys. Res. B 102 (1) (1995) 37–46.
[41] L.K. Béland, Y.N. Osetsky, R.E. Stoller, The effect of alloying nickel with iron on the supersonic ballistic stage of high energy displacement cascades, Acta Mater. 116 (2016) 136–142.
[42] L.K. Béland, C. Lu, Y.N. Osetsky, G.D. Samolyuk, R.E. Stoller, Features of primary damage by high energy displacement cascades in concentrated Ni-based alloys, J. Appl. Phys. 119 (8) (2016), 085901.
[43] L.K. Béland, Y.N. Osetsky, R.E. Stoller, Atomistic material behavior at extreme pressures, Npj Comput. Mater. 2 (2016) 16007.
[44] M.J. Banisalman, T. Oda, Atomistic simulation for strain effects on threshold displacement energies in refractory metals, Comput. Mater. Sci. 158 (2019) 346–352.
[45] C. Kang, Q. Wang, L. Shao, Kinetics of interstitial defects in α-fe: the effect from uniaxial stress, J. Nucl. Mater. 485 (2017) 159–168.
[46] F. Gao, D. Bacon, P. Flewitt, T. Lewis, A molecular dynamics study of temperature effects on defect production by displacement cascades in α-iron, J. Nucl. Mater. 249 (1) (1997) 77–86.
[47] C. Wang, W. Zhang, C. Ren, P. Huai, Z. Zhu, The effect of temperature on primary defect formation in Ni Fe alloy, Nucl. Instrum. Methods Phys. Res. B 321 (2014) 49–53.
[48] Z. Chen, N. Kioussis, N. Ghoniem, D. Seif, Strain-field effects on the formation and migration energies of self interstitials in α-Fe from first principles, Phys. Rev. B 81 (2010), 094102.